



Efficient NiFe-based oxygen evolution electrocatalysts and origin of their distinct activity

Qinglin Han^a, Yuhong Luo^a, Jingde Li^{a,*}, Xiaohang Du^{a,b}, Shujuan Sun^a, Yanji Wang^a, Guihua Liu^{a,*}, Zhongwei Chen^{b,*}

^a Hebei Provincial Key Laboratory of Green Chemical Technology and High Efficient Energy Saving, National-Local Joint Engineering Laboratory for Energy Conservation of Chemical Process Integration and Resources Utilization, Tianjin Key Laboratory of Chemical Process Safety, School of Chemical Engineering and Technology, Hebei University of Technology, Tianjin, 300130, China

^b Department of Chemical Engineering, University of Waterloo, Waterloo, ON, N2L 3G1, Canada

ARTICLE INFO

Keywords:

Bimetallic NiFe catalyst
Oxygen evolution reaction
Surface transition
In situ Raman
Density functional theory

ABSTRACT

Efficient oxygen evolution reaction (OER) electrocatalyst is essential for water electrolysis. Herein, high-performance NiFe-based layered double hydroxides (LDH), phosphide and sulfide OER pre-catalysts were fabricated and their distinct activity was unveiled. The as-prepared $\text{Ni}_x\text{Fe}_{1-x}\text{S}$ exhibits ultralow OER overpotential of 122 mV at 10 mA cm⁻² in 1 M KOH. The alkali-electrolyzer using $\text{Ni}_x\text{Fe}_{1-x}\text{S}$ electrodes achieve superior performance exhibiting a voltage of 1.46 V at 10 mA cm⁻². Experimental analysis reveals that, during OER, Fe dissolution into electrolyte occurs for NiFe LDH and $\text{Ni}_x\text{Fe}_{1-x}\text{P}$, which were both converted into NiOOH, well explaining their similar activity. Interestingly, Fe dissolution is significantly mitigated in $\text{Ni}_x\text{Fe}_{1-x}\text{S}$, forming partially oxidized $\text{Fe}_2\text{O}_3/\text{FeOOH}$ species. Theoretical calculations confirmed that $\text{Fe}_2\text{O}_3/\text{FeOOH}$ is responsible for the enhanced OER energetics of $\text{Ni}_x\text{Fe}_{1-x}\text{S}$. These observations provide new insights on the distinct activity of NiFe-based electrocatalysts, guiding their rational design as well.

1. Introduction

Electrically driven water splitting for hydrogen production is a promising clean energy technology [1–3]. In water electrolysis, oxygen evolution reaction (OER) is the key but slow process, hindering its overall energy conversion efficiency [4,5]. Therefore, the development of efficient and low-cost electrocatalysts for OER reaction is vital for the practical application of water electrolysis technology. NiFe-based layered double hydroxides (LDHs) are one of the most effective OER catalysts in alkaline media [6,7]. In addition, NiFe-based transition metal phosphides (TMPs) [8–10] and transition metal sulfides (TMSs) [11–13] were also demonstrated exhibiting excellent OER activity. In these NiFe bimetal-based electrocatalysts, the synergistic electronic interaction between Ni and Fe was usually considered plays an essential role in promoting the OER kinetics in water splitting [14–16].

Recently, there are increasing studies showing that, under the oxidation potential of OER reaction, the surface of NiFe-based TMPs and TMSs would convert into their corresponding oxyhydroxides and oxides [17,18]. Additionally, despite this in-situ oxidation reaction, these TMPs

and TMSs catalysts still exhibit excellent activity and stability performance during OER reaction, and sometime even show improved activity over the corresponding metal oxides and hydroxides-based catalysts [19–21]. The good catalytic performance of TMSs and TMPs has been attributed to their high conductivity [22,23], and the doping effect of S or P into the in-situ formed hydroxides surface, which tunes the valence state of Ni/Fe and therefore enhances its OER activity [24,25]. Despite of these achievements, there is always a demand for fabricating high-performance NiFe-based electrocatalysts. Also, their underlying origin that governs the distinct catalytic activity of these NiFe-based TMPs and TMSs was rarely reported. Such study would not only provide a comprehensive understanding on their intrinsic OER activity, but also guide the optimal design of efficient NiFe-based electrocatalysts.

In the present study, nickel foam supported high-performance NiFe LDH, $\text{Ni}_x\text{Fe}_{1-x}\text{P}$ and $\text{Ni}_x\text{Fe}_{1-x}\text{S}$ catalysts were successfully fabricated, and their distinct catalytic activity towards OER reaction was systematically investigated. Interesting, it is found that $\text{Ni}_x\text{Fe}_{1-x}\text{S}$ exhibits the highest OER activity, whereas the activity of NiFe LDH and $\text{Ni}_x\text{Fe}_{1-x}\text{P}$ is very similar. Therefore, $\text{Ni}_x\text{Fe}_{1-x}\text{S}$ only exhibits a 122 mV overpotential

* Corresponding authors.

E-mail addresses: jingdeli@hebut.edu.cn (J. Li), guihualiu@hebut.edu.cn (G. Liu), zhwchen@uwaterloo.ca (Z. Chen).



at 10 mA cm⁻², and the Ni_xFe_{1-x}S electrode only needs a cell voltage of 1.46 V to drive water electrolysis at 10 mA cm⁻². In-situ Raman, X-ray photoelectron spectroscopy (XPS) and transmission electron microscope (TEM) analysis of the post-OER samples reveal that, during the OER reaction, dissolution of Fe into the electrolyte occurs for NiFe LDH and Ni_xFe_{1-x}P, both of which are found in-situ oxidized into NiOOH, well explaining their similar OER activity. On the other hand, Fe dissolution is significantly mitigated in Ni_xFe_{1-x}S, and its partial oxidation into Fe₂O₃/FeOOH species is observed. Theoretical calculations show that, compared with NiOOH, the in-situ generated Fe₂O₃/FeOOH species possess promoted energetics towards the key OER elementary reaction steps and enhanced the electron localization function (ELF) of Fe-O bonds, contributing to the high activity of Ni_xFe_{1-x}S pre-catalyst. These observations provide new insights on the distinct origin activity of NiFe LDH, Ni_xFe_{1-x}P and Ni_xFe_{1-x}S towards OER reaction. This study also implies that the suppression of Fe dissolution and its appropriate activation through in-situ surface reconstruction might play a key role in the design of efficient NiFe-based electrocatalysts.

2. Experiment and computational details

2.1. Materials and reagent

Ferric nitrate [Fe(NO₃)₃·9H₂O], nickel nitrate [Ni(NO₃)₂·6H₂O], sodium hypophosphite (NaH₂PO₂·H₂O) and potassium hydroxide (KOH) were purchased from Aladdin Industrial Company. Nickel foam (NF, 1.0 mm thick) and carbon cloth (CC) were purchased from Shenzhen Lvchuang Environmental Technology Co. Ltd. Sulfur powder was obtained from commercial suppliers without further purification.

2.2. Material synthesis

Preparation of NiFe LDH. The electrodeposition process is conducted in a standard three-electrode electrochemical cell, with anodized nickel foam as the working electrode, carbon rod as the counter electrode, and saturated calomel electrode (SCE) as the reference electrode. The electrolyte contains 1.00 M Ni(NO₃)₂·6H₂O and 0.25 M Fe(NO₃)₃·9H₂O. Then, constant current electrodeposition is performed at 20 mA cm⁻² for a duration of 900 s. After rinsing with deionized water, the NiFe LDH product was obtained. In addition, by changing the ratio of Ni (NO₃)₂·6H₂O and Fe(NO₃)₃·9H₂O, NiFe LDH with different Ni:Fe ratio were synthesized under different electrodeposition current and duration. For comparison reason, samples without the addition of Fe (NO₃)₃·9H₂O or Ni(NO₃)₂·6H₂O were also synthesized, which were referred as Ni/NF and Fe/NF, respectively.

Preparation of Ni_xFe_{1-x}P and Ni_xFe_{1-x}S. The Ni_xFe_{1-x}P and Ni_xFe_{1-x}S pre-catalysts were prepared in a tube furnace. Specifically, for the preparation of Ni_xFe_{1-x}P, the above-prepared NiFe LDH and 0.5 g NaH₂PO₂·H₂O were placed in two separate porcelain bottles with a distance of 10 cm, and NaH₂PO₂·H₂O was placed at the upstream of the tube furnace. In Ar atmosphere, the furnace was heated from room temperature to 350 °C at a ramping rate of 2 °C min⁻¹ and was kept for 2 h. The resulting sample is Ni_xFe_{1-x}P. In addition, NiP and FeP was also developed as control samples by replacing NiFe LDH with Ni/NF and Fe/NF, respectively. For the synthesis of Ni_xFe_{1-x}S, the NaH₂PO₂·H₂O in the above step was replaced with sulfur powder. Then, the furnace was heated to 300 °C with a ramping rate of 2 °C min⁻¹ in Ar atmosphere and held for 3 h to obtain Ni_xFe_{1-x}S. The mass load of the Ni_xFe_{1-x}P and Ni_xFe_{1-x}S layer on the nickel foam is about 3.0 mg cm⁻². NiS and FeS were also developed for comparison by the same procedure using Ni/NF and Fe/NF, respectively.

2.3. Material characterization

The microstructure of the electrocatalysts was investigated by scanning electron microscope (SEM, Quanta 450 FEG) and TEM (JEOL

2010 F). Their crystal structure was studied by X-ray diffraction (XRD, D8 Discovery). In-situ Raman spectroscopy was recorded on the inVia Reflex instrument. XPS spectroscopy (ESCALAB 250 Xi) was used to characterize the chemical composition of these catalysts. Inductively coupled plasma (ICP) was performed on ICPE-9000 (detection limit: sub ppb). Standard solutions (TraceCERT) were purchased from Fluka (Sigma-Aldrich) and were used for calibration. Brunauer-Emmett-Teller (BET) (Autosorb iQ-MP-MP) adsorption isotherm was used to calculate the specific surface area.

2.4. Electrochemical measurements

The measurement of the electrolysis reaction was carried out using the CORRTEST CS2350 electrochemical workstation in a standard three-electrode system, in which NiFe LDH, Ni_xFe_{1-x}P and Ni_xFe_{1-x}S was used as the working electrode, carbon rod as the counter electrode, and Ag/AgCl as the reference electrode. Linear sweep voltammetry (LSV) curve detection range is 0–1 V (vs. Ag/AgCl), and the scan rate is 10 mV s⁻¹. The overpotential (η) of the catalysts were calculated using the equation $\eta = E_{\text{RHE}} - 1.23 \text{ V}$ [26]. The Tafel slope is calculated using the Tafel equation: $\eta = b \log j + a$, where η is the overpotential, j represents current density, and b is the Tafel slope [27]. The electrochemical impedance spectroscopy (EIS) analysis was performed at the different overpotential in the frequency range of 1000 kHz to 1 Hz. The electrochemical surface area (ECSA = C_{dL}/C_s) was evaluated using the cyclic voltammetry (CV) curves in the Faradaic reaction zone at different scanning rates (10–50 mV s⁻¹). C_s represents the specific capacitance of 1.0 M KOH (0.04 mF cm⁻²) [1]. The double-layer capacitance (C_{dL}) is calculated by: C_{dL} = j_c/V, where j_c represents the current density and V is the voltage [28]. The overall water splitting reaction was performed in 1.0 M KOH at room temperature. The polarization curves were recorded by linear scanning voltammetry from 1.0 to 2.2 V with a scanning rate of 10 mV s⁻¹. The current density-time (i-t) curves of water electrolysis were measured at 1.93 V.

2.5. Density functional theory (DFT) calculation

The DFT calculations were carried out using the Vienna Ab initio Simulation Package (VASP), in which Blöchl's all-electron-like projector augmented wave (PAW) method [29,30] was implemented. Generalized gradient approximation (GGA)-based PBE-D3 functional [31] was selected. The kinetic plane-wave cutoff energy is set to 400 eV. The Brillouin zone is integrated using a 2 × 2 × 1 k-point mesh of Monkhorst Pack sets. The energy and force convergence criterion are set to 10⁻⁵ eV/atom and –0.03 eV/Å, respectively. Climbing image nudged elastic band (CI-NEB) method was adopted for the search of reaction transition states (TS) [32]. The adsorption and reaction kinetics were performed on the realistic catalytic phases revealed by in-situ Raman and post-OER HRTEM analysis. These include the NiOOH, FeOOH and the mixed valence Fe₂O₃/FeOOH species. The Fe₂O₃/FeOOH model was constructed on the basis of FeOOH model, in which the oxygen coordination state of selected surface Fe atoms was adjusted into Fe₂O₃.

3. Results and discussion

3.1. The structure and morphology of pre-electrocatalysts

The XRD patterns of NiFe LDH, Ni_xFe_{1-x}P and Ni_xFe_{1-x}S catalysts are shown in Fig. 1a. Metallic Ni phase was observed in all the samples, which is contributed by nickel foam substrate. No other crystalline was found for NiFe LDH. This is reasonable because NiFe LDH obtained by electrodeposition of Ni and Fe is usually difficult be detected by XRD analysis [33]. Therefore, XRD was used to verify the catalyst electro-deposited on the carbon cloth (CC) under the same conditions, and the diffraction peak of NiFe LDH was found (Fig. S1). The characteristic peak of Ni_xFe_{1-x}P reveals it is a composite of Ni₂P and Fe₂NiP

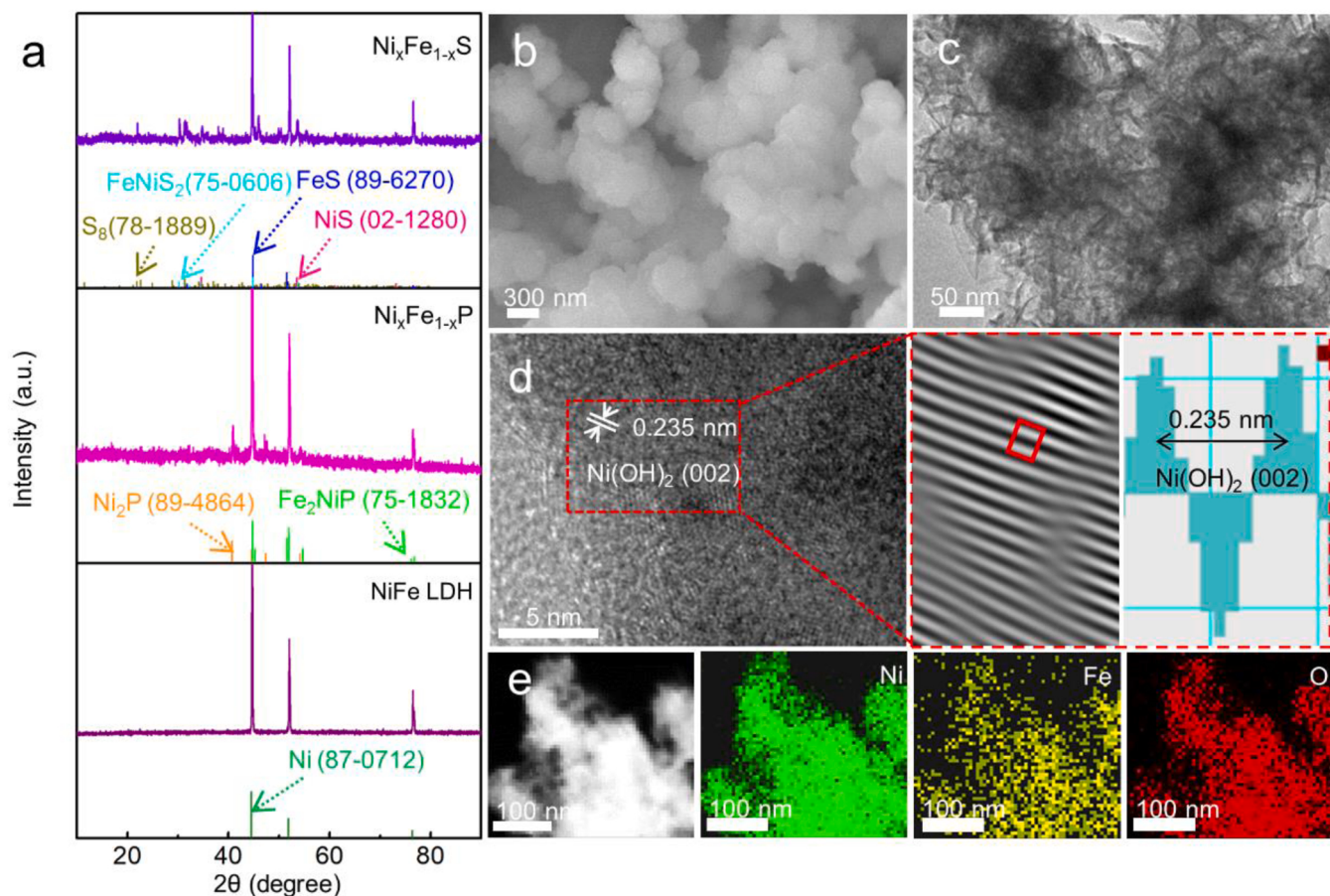


Fig. 1. (a) XRD patterns; (b) SEM image, (c) TEM image, (d) HRTEM image and (e) TEM mapping of NiFe LDH (before OER).

crystalline. In $\text{Ni}_x\text{Fe}_{1-x}\text{S}$, the NiS , FeS , FeNiS_2 and S_8 crystals were observed. The presence of S_8 might due to a thin layer of sulfur powder remaining on the surface of $\text{Ni}_x\text{Fe}_{1-x}\text{S}$ during sulfidation. The morphology and crystal structure of the NiFe LDH, $\text{Ni}_x\text{Fe}_{1-x}\text{P}$ and $\text{Ni}_x\text{Fe}_{1-x}\text{S}$ electrocatalysts (before OER) were further characterized by SEM and TEM imaging. Fig. S2 shows that NiFe LDH, $\text{Ni}_x\text{Fe}_{1-x}\text{P}$ and $\text{Ni}_x\text{Fe}_{1-x}\text{S}$ were uniformly grown on the nickel foam substrate. The SEM image in Fig. 1b shows that NiFe LDH is aggregated into nanoparticles in the size of around 300 nm. TEM analysis reveals that NiFe LDH has a two-dimensional (2D) nanosheet morphology (Fig. 1c). The high-resolution TEM (HRTEM) image of NiFe LDH shows the existence of $\text{Ni}(\text{OH})_2$ (002) plane with a lattice spacing of 0.235 nm (Fig. 1d). The element mapping image reveals that NiFe LDH has a uniform distribution of Ni, Fe, and O elements (Fig. 1e). The morphology of NiFe LDH remains intact after OER reaction (Fig. S3).

Fig. 2a shows the TEM image of $\text{Ni}_x\text{Fe}_{1-x}\text{P}$, which also exhibits a 2D nanosheet morphology. This is consistent with that observed in the SEM image of $\text{Ni}_x\text{Fe}_{1-x}\text{P}$ (Fig. S4a-b). The HRTEM image and reverse fast Fourier transform (FFT) image of the selected region of $\text{Ni}_x\text{Fe}_{1-x}\text{P}$ has a lattice fringe spacing of 0.202 and 0.211 nm, corresponding to the Ni_2P (201) and Fe_2NiP (112) plane, respectively (Fig. 2b, S4c-d). The presence of Ni_2P and Fe_2NiP crystals in $\text{Ni}_x\text{Fe}_{1-x}\text{P}$ are also confirmed by the SAED diffraction pattern (Fig. 2c). The TEM elemental mapping image reveals the uniform distribution of Ni, Fe and P element, further confirming the successful formation of $\text{Ni}_x\text{Fe}_{1-x}\text{P}$ (Fig. 2d). Interestingly, a uniform distribution of O element was also observed in the mapping image, which might result from the oxidation of $\text{Ni}_x\text{Fe}_{1-x}\text{P}$ when it was exposed in ambient air. After OER reaction, the morphology of $\text{Ni}_x\text{Fe}_{1-x}\text{P}$ was not changed (Fig. S5). The morphology and structure of $\text{Ni}_x\text{Fe}_{1-x}\text{S}$ is similar with that of NiFe LDH and $\text{Ni}_x\text{Fe}_{1-x}\text{P}$ (Fig. 2e, S6).

As shown in Fig. 2f, the HRTEM image of $\text{Ni}_x\text{Fe}_{1-x}\text{S}$ also possesses three lattice fringes: 0.202, 0.258 and 0.647 nm lattice fringes, corresponding to the (102) plane of FeNiS_2 , the NiS (101) and FeS (001) plane, respectively. This is also consistent with that revealed in the SAED diffraction pattern (Fig. 2g). Similar in that of $\text{Ni}_x\text{Fe}_{1-x}\text{P}$, TEM elemental mapping image of $\text{Ni}_x\text{Fe}_{1-x}\text{S}$ also shows the existence of O element, suggesting existence of surface oxidation (Fig. 2h). After OER reaction, the morphology and element distribution of $\text{Ni}_x\text{Fe}_{1-x}\text{S}$ remains almost unchanged (Fig. S7).

3.2. Electrochemical performance analysis

The OER activity of NiFe LDH, $\text{Ni}_x\text{Fe}_{1-x}\text{P}$ and $\text{Ni}_x\text{Fe}_{1-x}\text{S}$ was measured in 1.0 M KOH. Fig. S8a-c present the LSV curves of NiFe LDH samples prepared with different Ni:Fe ratios, electrodepositing current and duration. It was found that NiFe LDH with a molar ratio of Ni:Fe = 4:1 deposited under 20 mA cm⁻² for 15 min has the lowest overpotential for OER. Fig. 3a shows that, $\text{Ni}_x\text{Fe}_{1-x}\text{S}$ requires an OER overpotential of 122 mV to reach 10 mA cm⁻², which is lower than NiFe LDH (260 mV) and Ir/C (290 mV). $\text{Ni}_x\text{Fe}_{1-x}\text{P}$ shows obvious oxidation peak at 10 mA cm⁻². Note that, $\text{Ni}_x\text{Fe}_{1-x}\text{S}$ also shows higher OER performance than the other control samples as well (Fig. S8d). As shown in Fig. 3b, the overpotential required for $\text{Ni}_x\text{Fe}_{1-x}\text{S}$ to reach 200 mA cm⁻² is 441 mV, much lower than that of $\text{Ni}_x\text{Fe}_{1-x}\text{P}$ (528 mV), NiFe LDH (522 mV) and Ir/C (563 mV). Both $\text{Ni}_x\text{Fe}_{1-x}\text{P}$ and NiFe LDH require the same overpotential of 598 mV to reach 300 mA cm⁻², indicating similar OER activities of the two catalysts. The Tafel slope of $\text{Ni}_x\text{Fe}_{1-x}\text{S}$ (120 mV dec⁻¹) is also lower than $\text{Ni}_x\text{Fe}_{1-x}\text{P}$ (147 mV dec⁻¹), Ir/C (148 mV dec⁻¹) and NiFe LDH (146 mV dec⁻¹), indicating the OER reaction kinetics was accelerated on $\text{Ni}_x\text{Fe}_{1-x}\text{S}$ (Fig. 3c). In addition, the CV curves

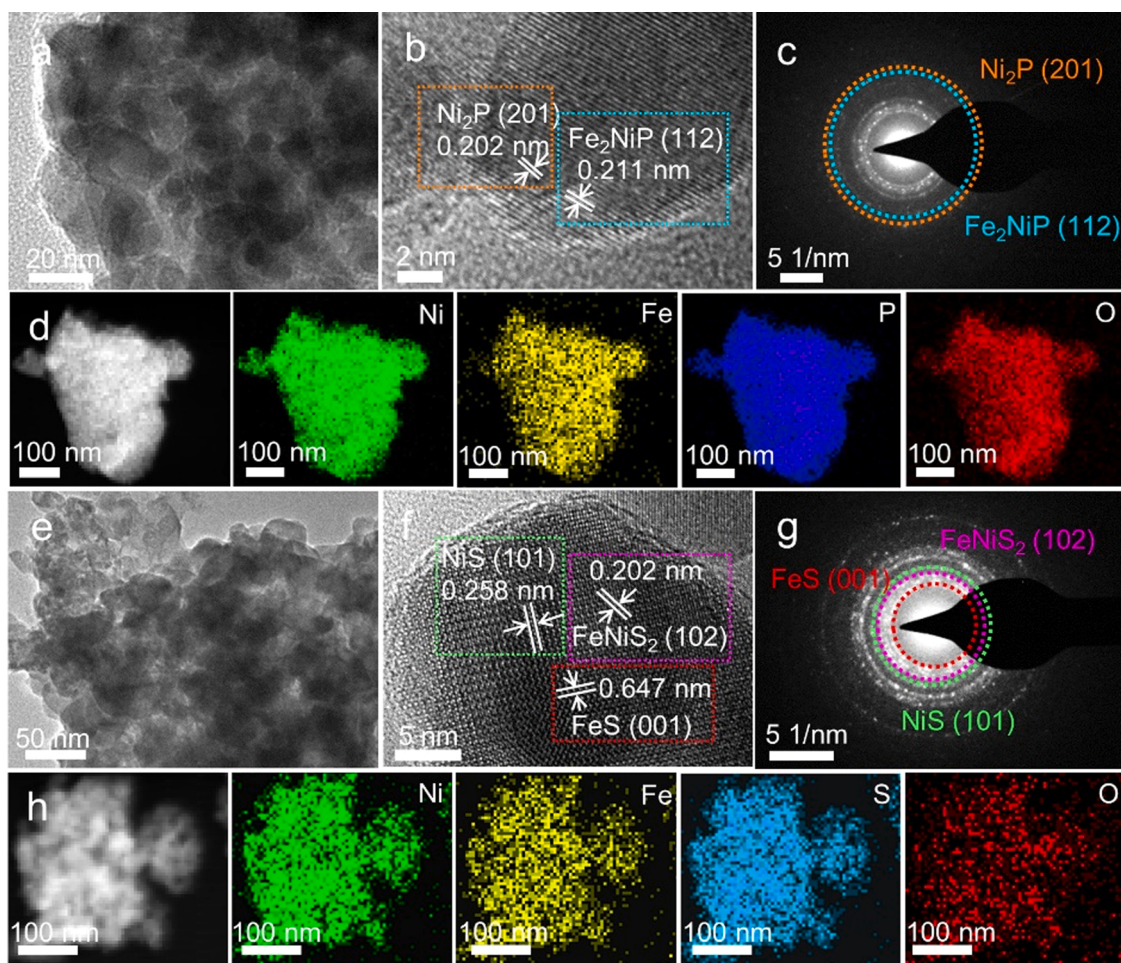


Fig. 2. (a) TEM image, (b) HRTEM image, (c) SAED pattern and (d) TEM mapping of $\text{Ni}_x\text{Fe}_{1-x}\text{P}$ (before OER); (e) TEM image, (f) HRTEM image, (g) SAED pattern and (h) TEM mapping of Ni, Fe, S and O elements in $\text{Ni}_x\text{Fe}_{1-x}\text{S}$ (before OER).

at different scan rates of NiFe LDH, $\text{Ni}_x\text{Fe}_{1-x}\text{P}$ and $\text{Ni}_x\text{Fe}_{1-x}\text{S}$ were measured to evaluate the ECSA of the three catalysts (Fig. S9). Fig. 3d shows that the corresponding C_{dl} of NiFe LDH, $\text{Ni}_x\text{Fe}_{1-x}\text{P}$ and $\text{Ni}_x\text{Fe}_{1-x}\text{S}$ are 44.4 mF cm^{-2} (ECSA = 1110 cm^2), 46.8 mF cm^{-2} (ECSA = 1170 cm^2) and 50.2 mF cm^{-2} (ECSA = 1255 cm^2), see Fig. S10. Meanwhile, the activity of the catalysts normalized by ECSA show a similar trend: $\text{Ni}_x\text{Fe}_{1-x}\text{S} > \text{Ni}_x\text{Fe}_{1-x}\text{P} \approx \text{NiFe LDH}$ (Fig. S11), suggesting that the increased activity of $\text{Ni}_x\text{Fe}_{1-x}\text{S}$ is indeed contributed by its intrinsic activity. In addition, the OER activities of NiFe LDH, $\text{Ni}_x\text{Fe}_{1-x}\text{P}$ and $\text{Ni}_x\text{Fe}_{1-x}\text{S}$ were also evaluated by the LSV curves normalized by BET surface area. As shown in Fig. S12, the specific surface areas of NiFe LDH, $\text{Ni}_x\text{Fe}_{1-x}\text{P}$ and $\text{Ni}_x\text{Fe}_{1-x}\text{S}$ are 23.62 , 8.92 and $3.99 \text{ cm}^3 \text{ g}^{-1}$, respectively. In comparison, $\text{Ni}_x\text{Fe}_{1-x}\text{S}$ still shows the highest current density after BET specific surface area normalization, demonstrating its highest OER activity among the three catalysts (Fig. S13). Fig. 3e shows the Nyquist diagram of NiFe LDH, $\text{Ni}_x\text{Fe}_{1-x}\text{P}$ and $\text{Ni}_x\text{Fe}_{1-x}\text{S}$ and the fitted equivalent circuit. One can see that all the electrodes present a typical half-arc Nyquist mode, where R_{ct} is the charge transfer resistance and R_s is the resistance of the solution. The R_{ct} of $\text{Ni}_x\text{Fe}_{1-x}\text{S}$ is 2.09Ω , which is smaller than that of $\text{Ni}_x\text{Fe}_{1-x}\text{P}$ (2.56Ω) and NiFe LDH (8.73Ω), indicating that $\text{Ni}_x\text{Fe}_{1-x}\text{S}$ has excellent charge transport capability. The i-t curves of NiFe LDH, $\text{Ni}_x\text{Fe}_{1-x}\text{P}$, $\text{Ni}_x\text{Fe}_{1-x}\text{S}$ and Ir/C electrodes were measured at 1.67 V (vs. RHE) for more than 25 h . The results show that $\text{Ni}_x\text{Fe}_{1-x}\text{S}$ exhibits higher and more stable current density compared to the other catalysts (Fig. 3f). The above analysis clearly demonstrated that the superior OER performance of $\text{Ni}_x\text{Fe}_{1-x}\text{S}$ catalyst even compared with that of recently reported electrocatalysts (Table S1).

3.3. Electrolysis of water

In view of the high catalytic activity of the $\text{Ni}_x\text{Fe}_{1-x}\text{S}$ and $\text{Ni}_x\text{Fe}_{1-x}\text{P}$ catalysts, their overall water electrolysis performance was evaluated. Fig. 4a is a schematic of water electrolysis experimental set up in 1.0 M KOH . For the $\text{Ni}_x\text{Fe}_{1-x}\text{S}$ electrode, to deliver a current density of 10 mA cm^{-2} , a battery voltage of 1.46 V was applied (Fig. 4b), which is lower than that of $\text{Ni}_x\text{Fe}_{1-x}\text{P}$ (1.60 V) and Ir/C // Pt/C (1.63 V) electrode. In addition, the overall water splitting activity of the alkaline electrolysis using $\text{Ni}_x\text{Fe}_{1-x}\text{S}$ catalyst outperforms most of the recently reported electrocatalysts (Table S2). Fig. 4c shows the i-t curves of $\text{Ni}_x\text{Fe}_{1-x}\text{P} // \text{Ni}_x\text{Fe}_{1-x}\text{P}$, $\text{Ni}_x\text{Fe}_{1-x}\text{S} // \text{Ni}_x\text{Fe}_{1-x}\text{S}$, and Ir/C // Pt/C electrodes operated at a potential of 1.93 V for 20 h . The analysis reveals that both $\text{Ni}_x\text{Fe}_{1-x}\text{P}$ and $\text{Ni}_x\text{Fe}_{1-x}\text{S}$ electrodes are more stable than Ir/C // Pt/C. These observations demonstrated that both $\text{Ni}_x\text{Fe}_{1-x}\text{P}$ and $\text{Ni}_x\text{Fe}_{1-x}\text{S}$ catalysts have good electrochemical activity and durability performance, and have the potential for large-scale applications. Fig. 4d is a demonstration of the water electrolysis process showing gas bubbles released at the electrodes. A video of this demonstration can be found in the Supporting Information. Finally, a drainage system is used to collect the gas and assess the overall water splitting process. As shown in Fig. S14, the collections of H_2 and O_2 evolve in a stoichiometric ratio of $2:1$. A acquisition of 13.7 mL O_2 was achieved in about 1200 s , with a Faradaic efficiency (FE) of nearly 99.78% (Fig. S15).

Supplementary material related to this article can be found online at doi:10.1016/j.apcatb.2021.120937.

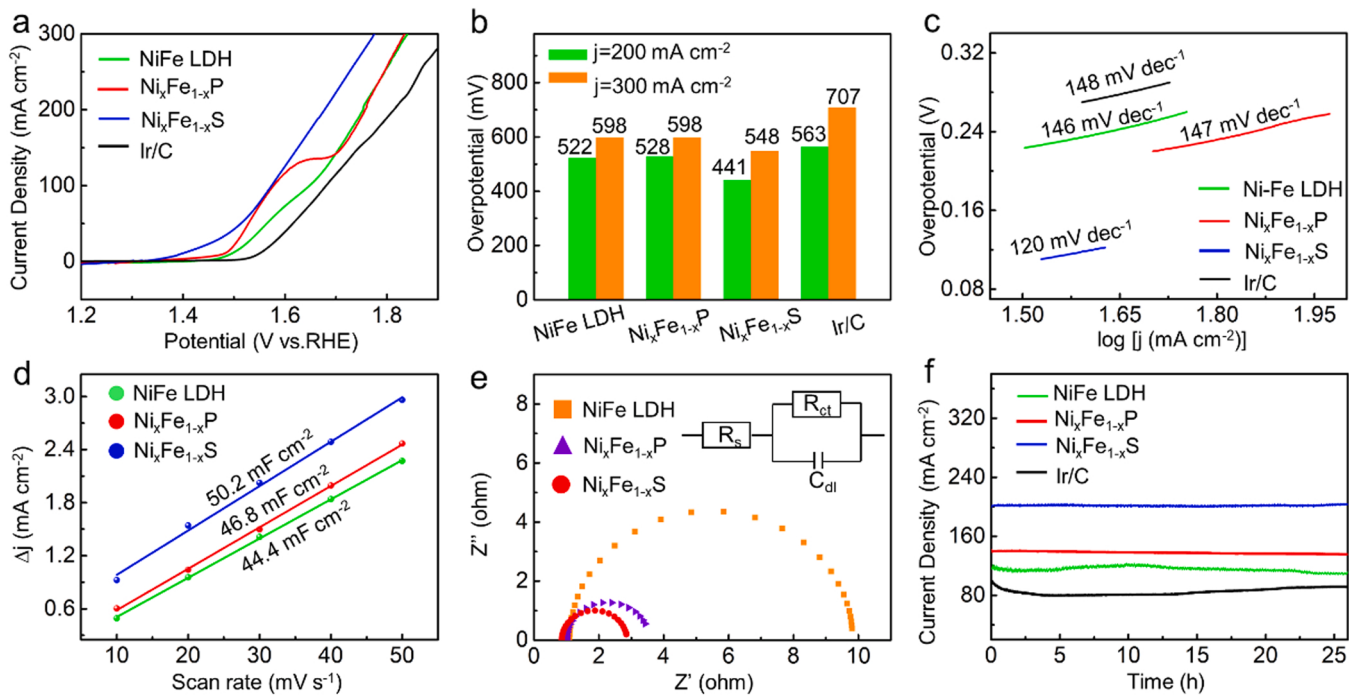


Fig. 3. Electrochemical measurements in 1 M KOH solution of different electrodes for OER reaction without iR correction. (a) LSV curves towards OER reaction obtained at the scan rate of 10 mV s⁻¹, (b) OER overpotentials at 200 and 300 mA cm⁻² and (c) Tafel diagram of NiFe LDH, Ni_xFe_{1-x}P, Ni_xFe_{1-x}S and Ir/C; (d) C_{dl}; (e) Nyquist plots; (f) i-t curves of NiFe LDH, Ni_xFe_{1-x}P, Ni_xFe_{1-x}S and Ir/C measured at 1.67 V (vs. RHE).

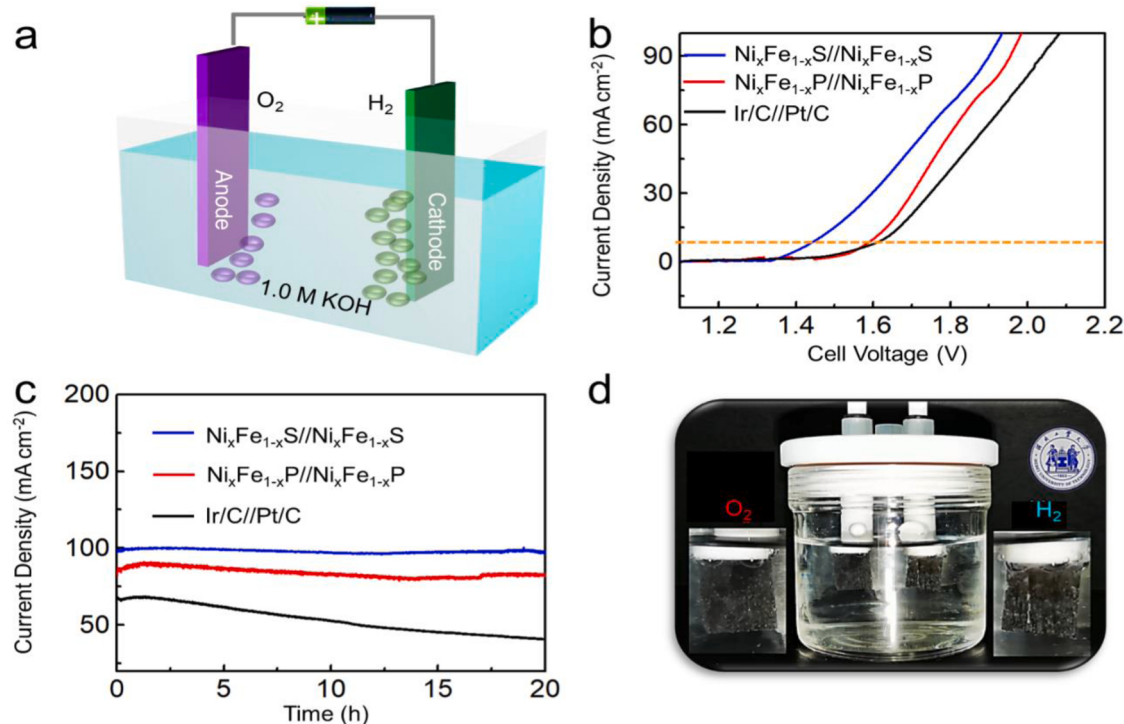


Fig. 4. (a) Schematic diagram of a two-electrode cell for electrolysis of water; (b) LSV curves and (c) i-t curves obtained at 1.93 V cell potential; (d) A photograph demonstrating the water electrolysis process.

3.4. Evolution of catalyst chemical state

To investigate the evolution of the chemical state of the catalyst surface in OER reaction, the XPS spectrum of Ni_xFe_{1-x}S, Ni_xFe_{1-x}P and NiFe LDH before and after OER reaction was compared. For Ni_xFe_{1-x}S

(before OER reaction), as shown in Fig. 5a, its Ni 2p spectrum exhibits two peaks located at 855.7 and 873.9 eV, which corresponding to the Ni 2p_{3/2} and Ni 2p_{1/2} state of Ni²⁺ species, respectively [34]. Its Fe 2p spectrum in Fig. 5b shows dominant peaks at 711.6 and 724.6 eV, corresponding to the Fe 2p_{3/2} and Fe 2p_{1/2} of Fe³⁺, respectively [35]. In

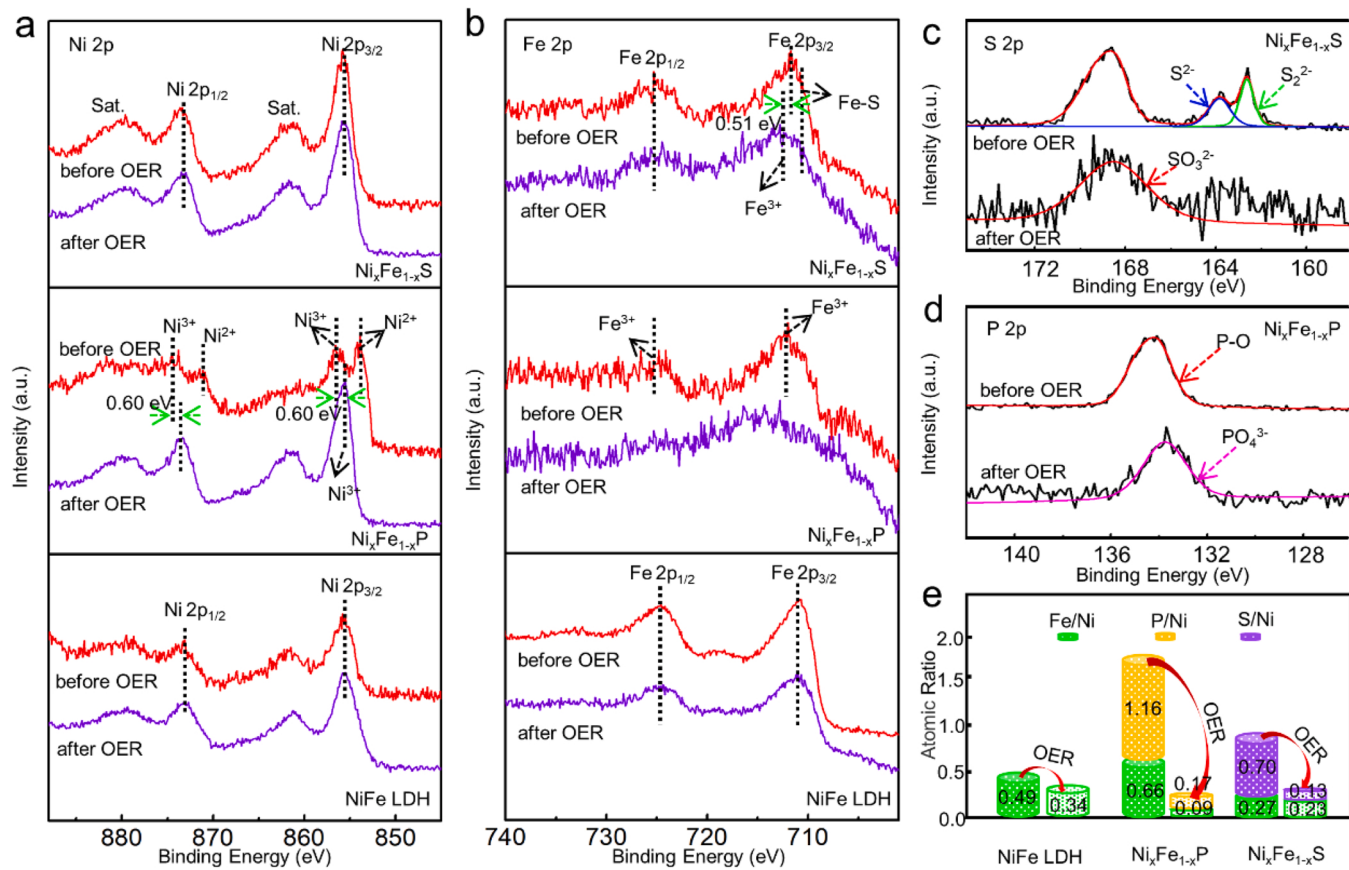


Fig. 5. High resolution XPS spectra of (a) Ni 2p and (b) Fe 2p for NiFe LDH, Ni_xFe_{1-x}P and Ni_xFe_{1-x}S; (c) P 2p of Ni_xFe_{1-x}P; (d) S 2p of Ni_xFe_{1-x}S; (e) Different atomic ratios before and after OER reaction by XPS with based on Ni.

addition, the Fe 2p spectrum also consists of the Fe-S state located at 710.3 eV [36]. In Fig. 5c, the S 2p spectrum exhibits two peaks at 162.3 and 163.4 eV correspond to S₂²⁻ and S²⁻, respectively, which is indicative for the existence of NiS, FeS and FeNiS₂ species [37,38]. The S 2p peak around 168.5 eV can be assigned to SO₃²⁻, which might resulted from the surface oxidation in ambient air [39]. After OER reaction, the following peak states/shifts were observed for Ni_xFe_{1-x}S: i) the Ni 2p peaks remain unchanged, suggesting its valence state was reserved during OER reaction; ii) the Fe 2p_{3/2} peak becomes broadened and slightly shifted towards higher binding energy, indicating a slight oxidation of Fe state during OER reaction; iii) the peaks of S₂²⁻ and S²⁻ disappears, implying that the sulfide on the catalyst surface was oxidized. For Ni_xFe_{1-x}P (before OER), in the Ni 2p spectrum (Fig. 5a), the peaks at 856.3 and 874.5 eV can be assigned to the Ni 2p_{3/2} and Ni 2p_{1/2} state of Ni³⁺-species, respectively, and the peak at 854.0 and 870.8 eV can be attributed to the Ni²⁺ species [34]. The Fe 2p spectrum of Ni_xFe_{1-x}P in Fig. 5b exhibits two main peaks at 711.9 and 724.6 eV, corresponding to the Fe 2p_{3/2} and Fe 2p_{1/2} of Fe³⁺, respectively. In Fig. 5d, the P 2p spectrum shows a P-O peak at 134.2 eV, which might resulted from the oxidation of phosphide exposed to air [40]. After OER test, the following peak shifts were observed for Ni_xFe_{1-x}P: i) the Ni²⁺ state disappears and the Ni 2p peaks shift towards higher binding energy, indicating its possible conversion into oxide/hydroxide [34]; ii) The Fe 2p signal after the OER reaction shows a shift toward higher binding energies and a significant decrease in spectral intensity, indicating Fe oxidation and possible dissolution in Ni_xFe_{1-x}P [41], the latter was proved by a Fe content of 0.985 mg/L in electrolyte determined by ICP measurement (Table S3); iii) a new peak at 133.6 eV appears, which is attributed to the formation of PO₄³⁻ species indicative for the oxidation of P component during OER reaction. In addition, the content of O after OER reaction is 51.2%, which is much higher than that before OER reaction (41.5%),

suggesting that the oxidation of Ni_xFe_{1-x}P is of high possibility. As for NiFe LDH (before OER), the two Ni 2p peaks (Fig. 5a) at 855.7 and 873.9 eV belong to the Ni 2p_{3/2} and Ni 2p_{1/2} states of Ni²⁺, respectively; the Fe 2p spectrum can be divided into Fe 2p_{3/2} and Fe 2p_{1/2} of Fe³⁺ at the two peaks of 710.1 and 725.0 eV respectively (Fig. 5b) [42]. After OER reaction: i) no peak shift in the Ni 2p and Fe 2p spectra was observed; ii) the weak signals of Fe 2p spectrum might resulted from the partially dissolution of Fe into electrolyte, which can be verified by the Fe contents in the electrolyte (Table S3). Furthermore, the change of surface Fe, S and P before and after OER reaction was quantified by their atomic ratios with Ni content determined by XPS analysis (Fig. 5e). Notably, the dissolution of Fe is observed for NiFe LDH (from 0.49 to 0.34) and particularly in Ni_xFe_{1-x}P (from 0.66 to 0.09). Note that, the severe Fe dissolution in Ni_xFe_{1-x}P was also accompanied by a significant decrease of P element from 1.16 to 0.17. On the other hand, although an apparent S dissolution was also observed for Ni_xFe_{1-x}S, the Fe dissolution is very minor (from 0.27 to 0.23). This suggests that the Fe is more stable in sulfide than hydroxides and phosphide form, and the stabilization effect of Fe on the Ni_xFe_{1-x}S surface might plays a critical role for its higher OER performance than that of NiFe LDH and Ni_xFe_{1-x}P.

In order to further probing the distinct catalytic origin for OER reaction, in-situ Raman characterization of the catalysts was performed. Fig. 6a shows the in-situ Raman spectra of the catalysts tested in 1.0 M KOH at different potentials. It can be seen that, when the working potential is in the range of OCV to 0.45 V, the surface species on NiFe LDH are Ni(OH)₂ (526 cm⁻¹) [43] and α-FeOOH (699 cm⁻¹) [44,45]. Interestingly, as the potential is increased to 0.50 V, the characteristics peaks of Ni(OH)₂ and α-FeOOH disappears. The disappearance of α-FeOOH might result from the Fe dissolution at the catalyst/electrolyte interface. At the same time, a new pair of frequency bands at 480 cm⁻¹ and 557 cm⁻¹ are formed, which can be attributed to the Ni-O vibration in

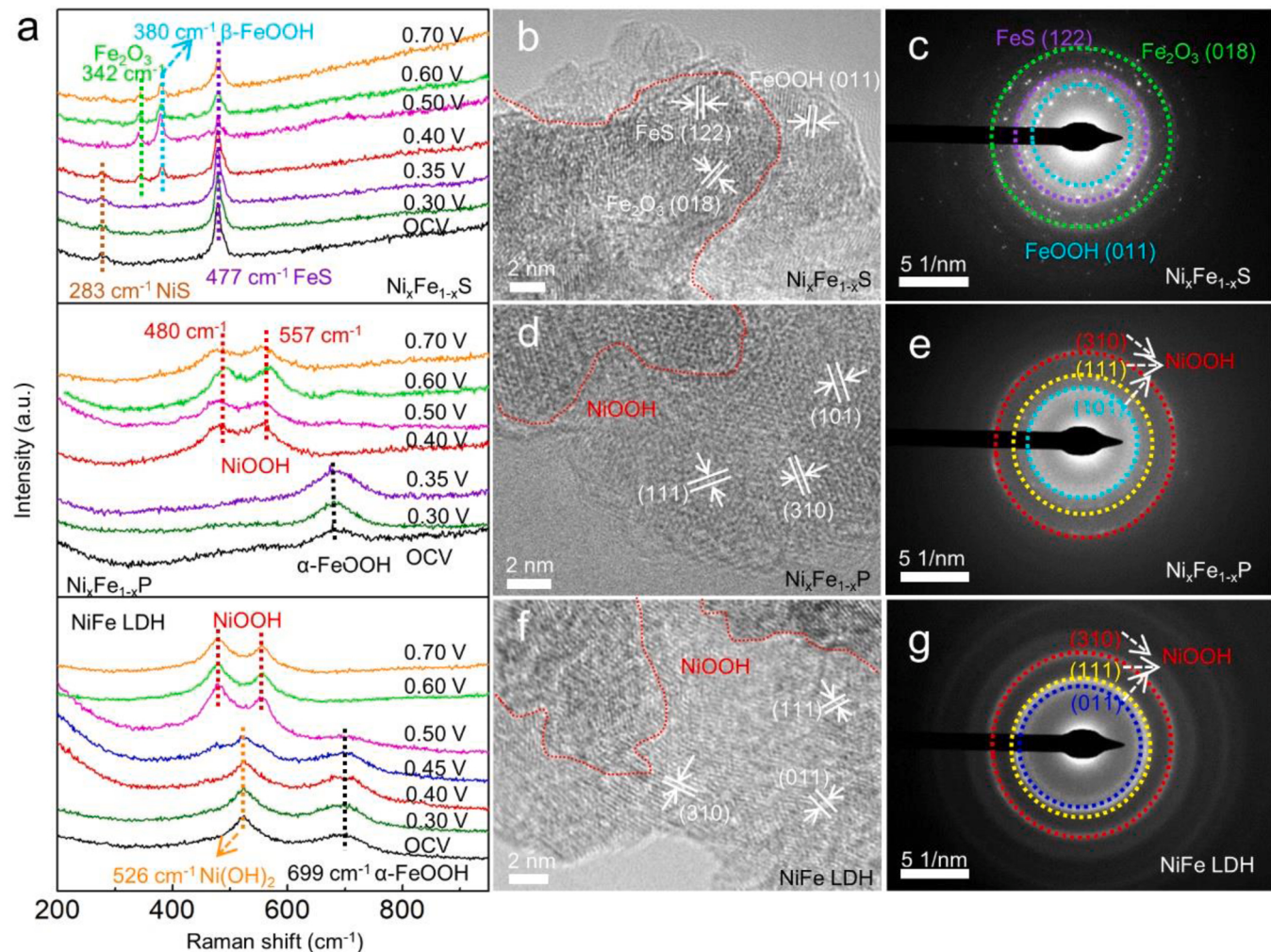


Fig. 6. (a) In-situ Raman of NiFe LDH, $\text{Ni}_x\text{Fe}_{1-x}\text{P}$ and $\text{Ni}_x\text{Fe}_{1-x}\text{S}$; (b) HRTEM image and (c) SAED pattern of $\text{Ni}_x\text{Fe}_{1-x}\text{S}$ after OER; (d) HRTEM image and (e) SAED pattern of $\text{Ni}_x\text{Fe}_{1-x}\text{P}$ after OER; (f) HRTEM image and (g) SAED pattern of NiFe LDH after OER reaction.

NiOOH [50]. This suggests that, at relatively high operating potentials, the OER catalytic active component of the NiFe LDH pre-catalyst is NiOOH. For $\text{Ni}_x\text{Fe}_{1-x}\text{P}$ pre-catalyst, when a working voltage of below 0.35 V is applied, only the characteristic peak of α -FeOOH is observed. As the voltage further increases, the α -FeOOH peak in $\text{Ni}_x\text{Fe}_{1-x}\text{P}$ disappears and new peaks corresponding to NiOOH was formed. This is similar with that observed for NiFe LDH. That is, regardless of the pre-catalysts state, the real catalytic component of NiFe LDH and $\text{Ni}_x\text{Fe}_{1-x}\text{P}$ towards OER reaction is NiOOH. This well explains the similar OER activity of NiFe LDH and $\text{Ni}_x\text{Fe}_{1-x}\text{P}$ observed in the electrochemical analysis (Fig. 3a). Notably, different with that of NiFe LDH and $\text{Ni}_x\text{Fe}_{1-x}\text{P}$, the in-situ Raman spectroscopy of $\text{Ni}_x\text{Fe}_{1-x}\text{S}$ shows distinct peaks and evolution behaviors: at voltages below 0.35 V, it only shows the NiS (283 cm^{-1}) [46] and FeS (477 cm^{-1}) [47] species. When the voltage increases to 0.40 V and above, partial oxidation of FeS into Fe₂O₃ (342 cm^{-1}) and β -FeOOH (380 cm^{-1}) is observed [48,49]. This implies that the existence of Fe₂O₃ and FeOOH on $\text{Ni}_x\text{Fe}_{1-x}\text{S}$ surface might lead to a synergistic catalytic effect and therefore benefit its OER performance. The partial oxidation of FeS also suggests that the sulfide-based pre-catalysts should be more resistance to oxidation than LDH and phosphide. Moreover, the HRTEM images of the three post-OER catalysts tend to form an amorphous phase (Fig. 6b, d and f). After OER reaction, NiOOH formation is observed in both NiFe LDH and $\text{Ni}_x\text{Fe}_{1-x}\text{P}$. For $\text{Ni}_x\text{Fe}_{1-x}\text{S}$ catalyst, in addition to the formation of FeOOH and Fe₂O₃, the existence of FeS can be still observed, which is in accord

with their corresponding SAED patterns (Fig. 6c, g and e). The existence of FeS further confirms the partial conversion of $\text{Ni}_x\text{Fe}_{1-x}\text{S}$, which is consistent with the in-situ Raman analysis.

3.5. DFT study on the origin of OER activity

Based on the results revealed by in-situ Raman analysis, the OER reaction kinetics on the realistic catalytic phase models, including NiOOH, FeOOH and Fe₂O₃/FeOOH, was investigated by DFT calculations. The Fe-S bonding observed in in-situ Raman analysis is not considered in the present Fe₂O₃/FeOOH model, because it is generally assumed that the oxidized and -OOH surface would eventually play a more significant effect in catalyzing OER reaction. Also, it is well-known that, in alkaline solution, OER reaction proceeds with a four electrons pathway (Supporting Information). In order to simply the calculation, only the key OER elementary reactions including the OH⁻ adsorption, *O, *OOH and *O₂ formation steps were considered [50,51]. Fig. S16 shows that, the adsorption energy (E_{ads}) of OH⁻ adsorption on Fe₂O₃/FeOOH model is found to be -3.02 eV (step 1). This strong adsorption energy suggests that OH⁻ adsorption step is very favorable to occur on the mixed valence Fe₂O₃/FeOOH surface. Interestingly, after optimizing the OH⁻ adsorption configuration on NiOOH, it was found directly reacts with the H on the surface of NiOOH forming H₂O molecule (step 2). Similar phenomenon also occurs for OH⁻ adsorption on FeOOH. These results show that OH⁻ adsorption could readily occurs on the NiOOH and

FeOOH surface, which is also beneficial to the OER process. In addition, this process on FeOOH have a lower reaction energy ($\Delta H = -2.04$ eV) than that of NiOOH ($\Delta H = -1.03$ eV), implying that the FeOOH might be more active towards OER reaction. Fig. 7a shows the TS of *OH transition into *O process on the three catalyst models. During this transition, the H atom in OH approaches the adjacent O atom forming O-H bond in the TS. The energy barriers of this reaction step on NiOOH, FeOOH and $\text{Fe}_2\text{O}_3/\text{FeOOH}$ were found to be 0.66, 0.58 and 0.21 eV, respectively. The corresponding ΔH is -0.82 , -3.76 and -0.90 eV, respectively. The low energy barrier on $\text{Fe}_2\text{O}_3/\text{FeOOH}$ suggests that the *OH to *O transition step is kinetically promoted than that on FeOOH and NiOOH. Similarly, the activation energies of the other two OER steps were also calculated. In the reaction of *OOH generation, the energy barrier of $\text{Fe}_2\text{O}_3/\text{FeOOH}$ is only 0.22 eV, which is much lower than that of FeOOH (0.46 eV) and NiOOH (0.53 eV), and their corresponding ΔH are -0.32 , -1.07 and -0.11 eV, respectively (Fig. 7 b). In the reaction of * O_2 production from *OOH, both $\text{Fe}_2\text{O}_3/\text{FeOOH}$ and FeOOH present an energy barrier of 0.40 eV, superior to NiOOH (0.81 eV). Although $\text{Fe}_2\text{O}_3/\text{FeOOH}$ exhibits the same kinetic energy barrier with FeOOH, the * O_2 formation step on $\text{Fe}_2\text{O}_3/\text{FeOOH}$ is thermodynamically more favorable due to the more negative ΔH of -2.99 eV than that of FeOOH (-2.63 eV), see Fig. 7c. Fig. 7d presents the ELF of Ni-O bond in NiOOH (0.56), the Fe-O bond in FeOOH (0.61) and $\text{Fe}_2\text{O}_3/\text{FeOOH}$ (0.66). The high ELF of Fe-O bond leads to more negative charge on the O atoms and more positive charge on the Fe atoms. This high ELF would improve the bonding between Fe and OER intermediates, and therefore lead to an enhanced oxygen evolution performance [52]. That is, $\text{Fe}_2\text{O}_3/\text{FeOOH}$ is predicted be more active than NiOOH and FeOOH

towards OER reaction. This explains the promoted OER activity on $\text{Ni}_x\text{Fe}_{1-x}\text{S}$ pre-catalyst, on which the $\text{Fe}_2\text{O}_3/\text{FeOOH}$ species was in-situ generated.

Fig. 8 is a schematic showing the surface reconstruction of NiFe LDH, $\text{Ni}_x\text{Fe}_{1-x}\text{P}$ and $\text{Ni}_x\text{Fe}_{1-x}\text{S}$ electrocatalysts during OER reaction. Briefly, when immersed in the alkaline electrolyte at open circuit voltage (OCV), $\text{Ni}(\text{OH})_2$ and FeOOH components were observed on NiFe LDH surface, whereas only FeOOH species was detected on $\text{Ni}_x\text{Fe}_{1-x}\text{P}$ pre-catalyst. When the OER working potentials were applied, both NiFe LDH and $\text{Ni}_x\text{Fe}_{1-x}\text{P}$ were found gradually converted into NiOOH species. Considering the same transition in OER reaction, an important implication is that NiFe LDH and $\text{Ni}_x\text{Fe}_{1-x}\text{P}$ might exhibit similar OER activity. On the other hand, for $\text{Ni}_x\text{Fe}_{1-x}\text{S}$ pre-catalyst, it was found mainly composed of NiS and FeS at OCV condition. During OER reaction, $\text{Ni}_x\text{Fe}_{1-x}\text{S}$ was partially oxidized to FeOOH and Fe_2O_3 without the observation of Ni-based species. These results unveiled the underlying origin that governs the distinct catalytic activity of NiFe-based electrocatalysts.

4. Conclusion

In the present study, high-performance NiFe-based electrocatalysts were fabricated on nickel foam using electrodeposition and chemical vapor deposition technique method. In order to unveil the distinct activity origin of NiFe LDH, $\text{Ni}_x\text{Fe}_{1-x}\text{P}$ and $\text{Ni}_x\text{Fe}_{1-x}\text{S}$ towards OER reaction, a systematic study on the evolution of the catalysts chemical states were presented. Electrochemical analysis shows that $\text{Ni}_x\text{Fe}_{1-x}\text{S}$ requires an OER overpotential of 441 mV to reach 200 mA cm⁻². It is much

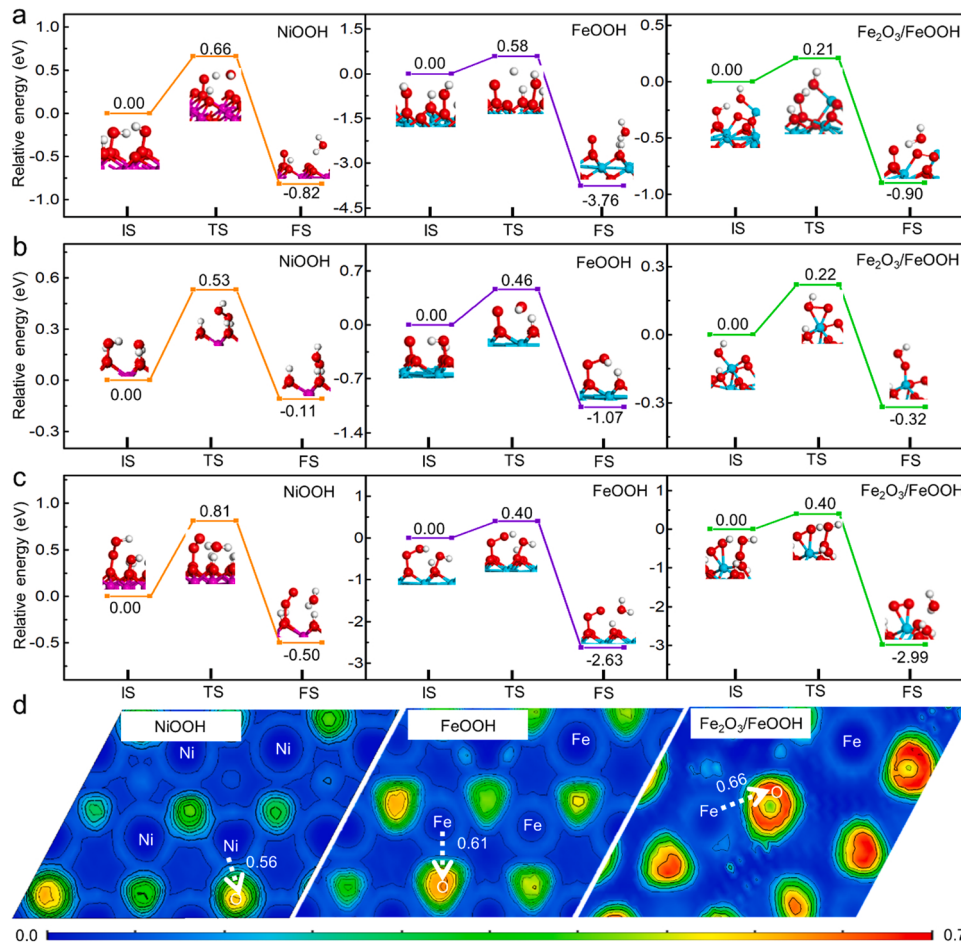


Fig. 7. The energy barriers for (a) *OH to *O transition reaction step: $*\text{OH} + \text{OH} \rightarrow *\text{O} + \text{H}_2\text{O} + \text{e}^-$; (b) *O to *OOH transition reaction step: $*\text{O} + \text{OH} \rightarrow *\text{OOH} + \text{e}^-$; (c) the *OOH to * O_2 transition reaction step: $*\text{OOH} + \text{OH} \rightarrow *\text{O}_2 + \text{H}_2\text{O} + \text{e}^-$ and (d) ELF on NiOOH, FeOOH and $\text{Fe}_2\text{O}_3/\text{FeOOH}$.

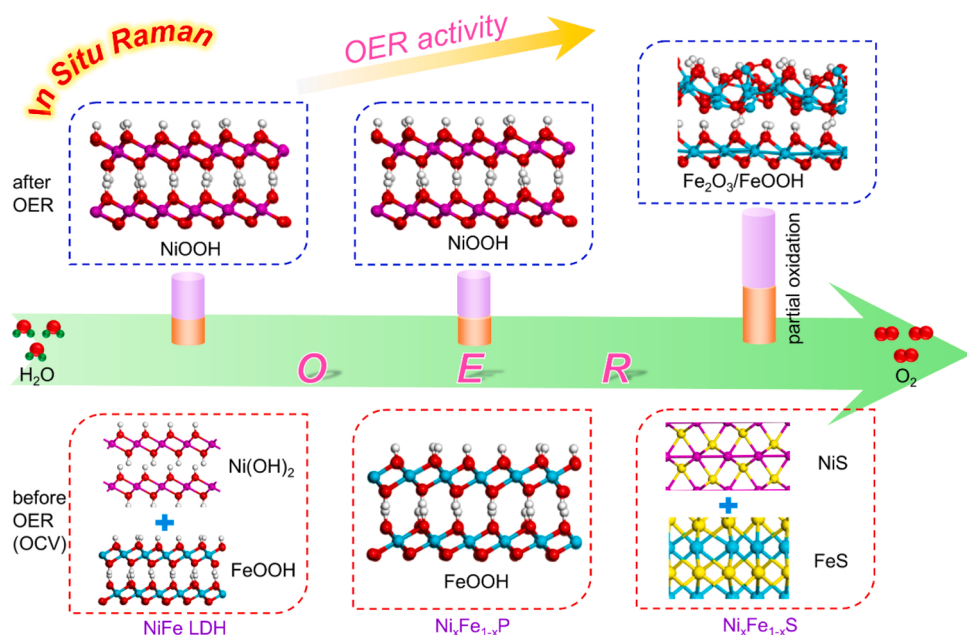


Fig. 8. Schematic of the transition of NiFe LDH, Ni_xFe_{1-x}P and Ni_xFe_{1-x}S in catalyzing OER reaction revealed by in-situ Raman spectroscopy. OCV is at open circuit voltage before OER reaction.

lower than Ni_xFe_{1-x}P (528 mV), NiFe LDH (522 mV). The alkali-electrolyzer using Ni_xFe_{1-x}S electrodes displays a cell voltage of 1.46 V to provide a current density of 10 mA cm⁻², outperforming the most reported electrocatalysts. On the basis of their electrochemical performance, the evolution and distinct activity of these pre-catalysts were comprehensively investigated by in-situ Raman spectroscopy, XPS and TEM analysis before and after OER reaction. The results that, during OER reaction, Ni(OH)₂ and α -FeOOH species were initially observed on NiFe LDH, and gradually oxidized to NiOOH at 0.50 V and above; Ni_xFe_{1-x}P is converted into α -FeOOH at voltages below 0.35 V, and transform into NiOOH at voltages above 0.35 V. The disappearance of α -FeOOH in NiFe LDH and Ni_xFe_{1-x}P at high working potentials was resulted from the dissolution of surface Fe into the electrolyte. Interestingly, the dissolution of Fe in Ni_xFe_{1-x}S is significantly mitigated. Accordingly, Ni_xFe_{1-x}S was partially oxidized into β -FeOOH and Fe₂O₃ at potentials above 0.35 V. DFT calculations reveal that the promoted OER energetics and enhanced electron localization function of Fe-O bonds on Fe₂O₃/FeOOH is responsible for the high activity of Ni_xFe_{1-x}S catalyst. This study unveiled the distinct intrinsic activity of NiFe LDH, Ni_xFe_{1-x}P and Ni_xFe_{1-x}S OER electrocatalysts, and provides guidance for the rational design and optimization of efficient transition metal-based OER electrocatalysts.

CRediT authorship contribution statement

Jingde Li, Guihua Liu and Zhongwei Chen: Conceptualization, Methodology, Supervision ; Qinglin Han: Investigation, Writing – original draft preparation; Yuhong Luo, Xiaohang Du, Shujuan Sun and Jingde Li: Visualization, Data analysis ; Guihua Liu, Yanji Wang and Zhongwei Chen: Writing – review & editing.

Declaration of Competing Interest

The authors declare that there are no known competing financial interests.

Acknowledgments

This work was supported by the National Natural Science Foundation

of China (21908039, 52102236), ‘Hundred Talents Program’ of Hebei Province (E2019050013), Overseas Education Faculty Supporting Project in Hebei Province (C20210335), the Outstanding Young Talents Project of Hebei High Education Institutions (BJ2019013), and Natural Science Foundation of Hebei Province (B2019202199, B2020202009, B2020202069).

Appendix A. Supporting information

Supplementary data associated with this article can be found in the online version at doi:10.1016/j.apcatb.2021.120937.

References

- [1] S. Sun, X. Zhou, B. Cong, W. Hong, G. Chen, Tailoring the d-band centers endows (Ni_xFe_{1-x})₂P nanosheets with efficient oxygen evolution catalysis, ACS Catal. 10 (2020) 9086–9097, <https://doi.org/10.1021/acscatal.0c01273>.
- [2] Z. Kou, Y. Yu, X. Liu, X. Gao, L. Zheng, H. Zou, Y. Pang, Z. Wang, Z. Pan, J. He, S. J. Pennycook, J. Wang, Potential-dependent phase transition and Mo-enriched surface reconstruction of γ -CoOOH in a heterostructured Co-Mo₂C precatalyst enable water oxidation, ACS Catal. 10 (2020) 4411–4419, <https://doi.org/10.1021/acscatal.0c00340>.
- [3] W. Zhu, W. Chen, H. Yu, Y. Zeng, F. Ming, H. Liang, Z. Wang, NiCo/NiCo-OH and NiFe/NiFe-OH core shell nanostructures for water splitting electrocatalysis at large currents, Appl. Catal. B-Environ. 278 (2020), 119326, <https://doi.org/10.1016/j.apcatb.2020.119326>.
- [4] C. Feng, M.B. Faheem, J. Fu, Y. Xiao, C. Li, Y. Li, Fe-based electrocatalysts for oxygen evolution reaction: progress and perspectives, ACS Catal. 10 (2020) 4019–4047, <https://doi.org/10.1021/acscatal.9b05445>.
- [5] J. Li, R. Lian, J. Wang, S. He, S.P. Jiang, Z. Rui, Oxygen vacancy defects modulated electrocatalytic activity of iron-nickel layered double hydroxide on Ni foam as highly active electrodes for oxygen evolution reaction, Electrochim. Acta 331 (2020), 135395, <https://doi.org/10.1016/j.electacta.2019.135395>.
- [6] Y. Yang, L. Dang, M.J. Shearer, H. Sheng, W. Li, J. Chen, P. Xiao, Y. Zhang, R. J. Hamers, S. Jin, Highly active trimetallic NiFeCr layered double hydroxide electrocatalysts for oxygen evolution reaction, Adv. Energy Mater. 8 (2018), 1703189, <https://doi.org/10.1002/aenm.201703189>.
- [7] J. Chen, F. Zheng, S.-J. Zhang, A. Fisher, Y. Zhou, Z. Wang, Y. Li, B.-B. Xu, J.-T. Li, S.-G. Sun, Interfacial interaction between FeOOH and Ni-Fe LDH to modulate the local electronic structure for enhanced OER electrocatalysis, ACS Catal. 8 (2018) 11342–11351, <https://doi.org/10.1021/acscatal.8b03489>.
- [8] H. Liang, A.N. Gandi, D.H. Anjum, X. Wang, U. Schwingenschlogl, H.N. Alshareef, Plasma-assisted synthesis of NiCoP for efficient overall water splitting, Nano Lett. 16 (2016) 7718–7725, <https://doi.org/10.1021/acs.nanolett.6b03803>.
- [9] Y. Pei, Y. Cheng, J. Chen, W. Smith, P. Dong, P.M. Ajayan, M. Ye, J. Shen, Recent developments of transition metal phosphides as catalysts in the energy conversion

- field, J. Mater. Chem. A 6 (2018) 23220–23243, <https://doi.org/10.1039/C8TA09454C>.
- [10] Y. Li, Z. Dong, L. Jiao, Multifunctional transition metal-based phosphides in energy-related electrocatalysis, Adv. Energy Mater. 10 (2019), 1902104, <https://doi.org/10.1002/aenm.201902104>.
- [11] X. Cheng, C. Lei, J. Yang, B. Yang, Z. Li, J. Lu, X. Zhang, L. Lei, Y. Hou, K. Ostrikov, Efficient electrocatalytic oxygen evolution at extremely high current density over 3D ultrasmall zero-valent iron-coupled nickel sulfide nanosheets, ChemElectroChem 5 (2018) 3866–3872, <https://doi.org/10.1002/celc.201801104>.
- [12] S. Chandrasekaran, L. Yao, L. Deng, C. Bowen, Y. Zhang, S. Chen, Z. Lin, F. Peng, P. Zhang, Recent advances in metal sulfides: from controlled fabrication to electrocatalytic, photocatalytic and photoelectrochemical water splitting and beyond, Chem. Soc. Rev. 48 (2019) 4178–4280, <https://doi.org/10.1039/C8CS00664D>.
- [13] Y. Guo, T. Park, J.W. Yi, J. Henzie, J. Kim, Z. Wang, B. Jiang, Y. Bando, Y. Sugahara, J. Tang, Y. Yamauchi, Nanoarchitectonics for transition-metal-sulfide-based electrocatalysts for water splitting, Adv. Mater. 31 (2019), 1807134, <https://doi.org/10.1002/adma.201807134>.
- [14] Y. Li, C. Zhao, Iron-doped nickel phosphate as synergistic electrocatalyst for water oxidation, Chem. Mater. 28 (2016) 5659–5666, <https://doi.org/10.1021/acs.chemmater.6b01522>.
- [15] Z. Zhao, H. Wu, H. He, X. Xu, Y. Jin, Self-standing non-noble metal (Ni–Fe) oxide nanotube array anode catalysts with synergistic reactivity for high-performance water oxidation, J. Mater. Chem. A 3 (2015) 7179–7186, <https://doi.org/10.1039/C5TA00160A>.
- [16] H. Xiao, H. Shin, W.A. Goddard 3rd, Synergy between Fe and Ni in the optimal performance of (Ni,Fe)OOH catalysts for the oxygen evolution reaction, Proc. Natl. Acad. Sci. 115 (2018) 5872–5877, <https://doi.org/10.1073/pnas.1722034115>.
- [17] L. Zhou, M. Shao, M. Wei, X. Duan, Advances in efficient electrocatalysts based on layered double hydroxides and their derivatives, J. Energy Chem. 26 (2017) 1094–1106, <https://doi.org/10.1016/j.jecchem.2017.09.015>.
- [18] R. Farhat, J. Dhainay, L.I. Halaoui, OER catalysis at activated and codeposited NiFe-Oxo/hydroxide thin films is due to postdeposition surface-Fe and is not sustainable without Fe in solution, ACS Catal. 10 (2019) 20–35, <https://doi.org/10.1021/acscatal.9b02580>.
- [19] J. Xu, J. Li, D. Xiong, B. Zhang, Y. Liu, K.H. Wu, I. Amorim, W. Li, L. Liu, Trends in activity for the oxygen evolution reaction on transition metal (M = Fe, Co, Ni) phosphide pre-catalysts, Chem. Sci. 9 (2018) 3470–3476, <https://doi.org/10.1039/C7SC05033J>.
- [20] W. Li, D. Xiong, X. Gao, L. Liu, The oxygen evolution reaction enabled by transition metal phosphide and chalcogenide pre-catalysts with dynamic changes, Chem. Commun. (Camb.) 55 (2019) 8744–8763, <https://doi.org/10.1039/C9CC02845E>.
- [21] K. Liu, F. Wang, P. He, T.A. Shifa, Z. Wang, Z. Cheng, X. Zhan, J. He, The role of active oxide species for electrochemical water oxidation on the surface of 3d-metal phosphides, Adv. Energy Mater. 8 (2018), 1703290, <https://doi.org/10.1002/aenm.201703290>.
- [22] L. Peng, S.S.A. Shah, Z. Wei, Recent developments in metal phosphide and sulfide electrocatalysts for oxygen evolution reaction, Chin. J. Catal. 39 (2018) 1575–1593, [https://doi.org/10.1016/S1872-2067\(18\)63130-4](https://doi.org/10.1016/S1872-2067(18)63130-4).
- [23] B.R. Wygant, K. Kawashima, C.B. Mullins, Catalyst or precatalyst? The effect of oxidation on transition metal carbide, pnictide, and chalcogenide oxygen evolution catalysts, ACS Energy Lett. 3 (2018) 2956–2966, <https://doi.org/10.1021/acsenergylett.8b01774>.
- [24] L. Yu, L. Wu, B. McElhenney, S. Song, D. Luo, F. Zhang, Y. Yu, S. Chen, Z. Ren, Ultrafast room-temperature synthesis of porous S-doped Ni/Fe (oxy)hydroxide electrodes for oxygen evolution catalysis in seawater splitting, Energy Environ. Sci. 13 (2020) 3439–3446, <https://doi.org/10.1039/D0EE00921K>.
- [25] X. Zhang, Y. Zhao, Y. Zhao, R. Shi, G.I.N. Waterhouse, T. Zhang, A simple synthetic strategy toward defect-rich porous monolayer NiFe-layered double hydroxide nanosheets for efficient electrocatalytic water oxidation, Adv. Energy Mater. 9 (2019), 1900881, <https://doi.org/10.1002/aenm.201900881>.
- [26] M. Yao, N. Wang, W. Hu, S. Komarneni, Novel hydrothermal electrodeposition to fabricate mesoporous film of $\text{Ni}_{0.8}\text{Fe}_{0.2}$ nanosheets for high performance oxygen evolution reaction, Appl. Catal. B-Environ. 233 (2018) 226–233, <https://doi.org/10.1016/j.apcatb.2018.04.009>.
- [27] H. Han, K.M. Kim, H. Choi, G. Ali, K.Y. Chung, Y.-R. Hong, J. Choi, J. Kwon, S. W. Lee, J.W. Lee, J.H. Ryu, T. Song, S. Mhin, Parallelized reaction pathway and stronger internal band bending by partial oxidation of metal sulfide-graphene composites: important factors of synergistic oxygen evolution reaction enhancement, ACS Catal. 8 (2018) 4091–4102, <https://doi.org/10.1021/acscatal.8b00017>.
- [28] G. Liu, J. Li, J. Fu, G. Jiang, G. Lui, D. Luo, Y.P. Deng, J. Zhang, Z.P. Cano, A. Yu, D. Su, Z. Bai, L. Yang, Z. Chen, An oxygen-vacancy-rich semiconductor-supported bifunctional catalyst for efficient and stable zinc-air batteries, Adv. Mater. 31 (2019), 1806761, <https://doi.org/10.1002/adma.201806761>.
- [29] K. Li, Y. Li, Y. Wang, F. He, M. Jiao, H. Tang, Z. Wu, The oxygen reduction reaction on Pt (111) and Pt (100) surfaces substituted by subsurface Cu: a theoretical perspective, J. Mater. Chem. A 3 (2015) 11444–11452, <https://doi.org/10.1039/C5TA01017A>.
- [30] X. Bai, E. Zhao, K. Li, Y. Wang, M. Jiao, F. He, X. Sun, H. Sun, Z. Wu, Theoretical investigation on the reaction pathways for oxygen reduction reaction on silicon doped graphene as potential metal-free catalyst, J. Electrochem. Soc. 163 (2016) F1496, <https://doi.org/10.1149/2.0381614jes>.
- [31] J.P. Perdew, K. Burke, M. Ernzerhof, Generalized gradient approximation made simple, Phys. Rev. Lett. 77 (1996) 3865, <https://doi.org/10.1103/PhysRevLett.77.3865>.
- [32] W. Li, G. Liu, J. Li, Y. Wang, L. Ricardez-Sandoval, Y. Zhang, Z. Zhang, Hydrogen evolution reaction mechanism on 2H-MoS₂ electrocatalyst, Appl. Surf. Sci. 498 (2019), 143869, <https://doi.org/10.1016/j.apsusc.2019.143869>.
- [33] L. Yu, H. Zhou, J. Sun, F. Qin, F. Yu, J. Bao, Y. Yu, S. Chen, Z. Ren, Cu nanowires shelled with NiFe layered double hydroxide nanosheets as bifunctional electrocatalysts for overall water splitting, Energy Environ. Sci. 10 (2017) 1820–1827, <https://doi.org/10.1039/C7EE01571B>.
- [34] Z. Qiu, Y. Ma, T. Edvinsson, In operando Raman investigation of Fe doping influence on catalytic NiO intermediates for enhanced overall water splitting, Nano Energy 66 (2019), 104118, <https://doi.org/10.1016/j.nanoen.2019.104118>.
- [35] P. Kaspar, D. Sobola, R. Dallaev, S. Ramazanov, A. Nebojsa, S. Rezaei, L. Grmela, Characterization of Fe₂O₃ thin film on highly oriented pyrolytic graphite by AFM, Ellipsometry and XPS, Appl. Surf. Sci. 493 (2019) 673–678, <https://doi.org/10.1016/j.apsusc.2019.07.058>.
- [36] J.C. Carver, G.K. Schweitzer, T.A. Carlson, Use of X-Ray photoelectron spectroscopy to study bonding in Cr, Mn, Fe, and Co compounds, J. Chem. Phys. 57 (1972) 973–982, <https://doi.org/10.1063/1.1678348>.
- [37] H. Konno, K. Sasaki, M. Tsunekawa, T. Takamori, R. Furuchi, X-ray photoelectron spectroscopic analysis of surface products on pyrite formed by bacterial leaching, Bunseki Kagaku 40 (1991) 609–616, https://doi.org/10.2116/bunseikagaku.40.11_609.
- [38] C. Karakaya, N. Solati, U. Savaci, E. Keleş, S. Turan, S. Çelebi, S. Kaya, Mesoporous thin-film NiS₂ as an idealized pre-electrocatalyst for a hydrogen evolution reaction, ACS Catal. 10 (2020) 15114–15122, <https://doi.org/10.1021/acscatal.0c03094>.
- [39] T. Tian, L. Huang, L. Ai, J. Jiang, Surface anion-rich NiS₂ hollow microspheres derived from metal-organic frameworks as a robust electrocatalyst for the hydrogen evolution reaction, J. Mater. Chem. A 5 (2017) 20985–20992, <https://doi.org/10.1039/C7TA06671F>.
- [40] Y. Wu, Y. Li, M. Yuan, Z. Liu, L. Xu, B. Wei, Direct growth of Ni-Fe phosphides nanohybrids on NiFe foam for highly efficient water oxidation, J. Alloy. Compd. 847 (2020), 156363, <https://doi.org/10.1016/j.jallcom.2020.156363>.
- [41] M. Qu, Y. Jiang, M. Yang, S. Liu, Q. Guo, W. Shen, M. Li, R. He, Regulating electron density of NiFe-P nanosheets electrocatalysts by a trifle of Ru for high-efficient overall water splitting, Appl. Catal. B-Environ. 263 (2020), 118324, <https://doi.org/10.1016/j.apcatb.2019.118324>.
- [42] X. Han, S. Wang, H. Huang, Y. Zhang, Hydroxyl radicals and sulfate radicals synergistically boosting the photocatalytic and mineralization ability of ¹D-²D Bi₅O₇/NiFe-LDH heterojunction, Appl. Surf. Sci. 540 (2021), 148237, <https://doi.org/10.1016/j.apsusc.2020.148237>.
- [43] G. Zhang, G. Wang, H. Liu, J. Qu, J. Li, Rapidly catalysis of oxygen evolution through sequential engineering of vertically layered FeNi structure, Nano Energy 43 (2018) 359–367, <https://doi.org/10.1016/j.nanoen.2017.11.035>.
- [44] Z. Qiu, Y. Ma, T. Edvinsson, In operando Raman investigation of Fe doping influence on catalytic NiO intermediates for enhanced overall water splitting, Nano Energy 66 (2019), 104118, <https://doi.org/10.1016/j.nanoen.2019.104118>.
- [45] D.L.A. De Faria, S. Venâncio Silva, M.T. De Oliveira, Raman microspectroscopy of some iron oxides and oxyhydroxides, J. Raman Spectrosc. 28 (1997) 873–878, [https://doi.org/10.1002/\(SICI\)1097-4555\(199711\)28:11<873::AID-JRS177>3.0.CO;2-B](https://doi.org/10.1002/(SICI)1097-4555(199711)28:11<873::AID-JRS177>3.0.CO;2-B).
- [46] K. Zhu, X. Zhu, W. Yang, Application of in situ techniques for the characterization of NiFe-based oxygen evolution reaction (OER) electrocatalysts, Angew. Chem. Int. Ed. Engl. 58 (2019) 1252–1265, <https://doi.org/10.1002/anie.201802923>.
- [47] G. Genchev, A. Erbe, Raman spectroscopy of Mackinawite FeS in anodic iron sulfide corrosion products, J. Electrochem. Soc. 163 (2016) C333–C338, (<http://creativecommons.org/licenses/by/4.0/>).
- [48] M.K. Nieuwoudt, J.D. Comins, I. Cukrowski, The growth of the passive film on iron in 0.05 M NaOH studied in situ by Raman micro-spectroscopy and electrochemical polarisation. Part I: near-resonance enhancement of the Raman spectra of iron oxide and oxyhydroxide compounds, J. Raman Spectrosc. 42 (2011) 1335–1339, <https://doi.org/10.1002/jrs.2837>.
- [49] J. Gui, T. Devine, The influence of sulfate ions on the surface enhanced Raman spectra of passive films formed on iron, Corros. Sci. 36 (1994) 441–462, [https://doi.org/10.1016/0010-938X\(94\)90036-1](https://doi.org/10.1016/0010-938X(94)90036-1).
- [50] Z. Xue, X. Zhang, J. Qin, R. Liu, Revealing Ni-based layered double hydroxides as high-efficiency electrocatalysts for the oxygen evolution reaction: a DFT study, J. Mater. Chem. A 7 (2019) 23091–23097, <https://doi.org/10.1039/C9TA06686A>.
- [51] Y. Lin, Z. Liu, L. Yu, G.R. Zhang, H. Tan, K.H. Wu, F. Song, A.K. Mechler, P.P. M. Schleker, Q. Lu, B. Zhang, S. Heumann, Overall oxygen electrocatalysis on nitrogen-modified carbon catalysts: identification of active sites and in situ observation of reactive intermediates, Angew. Chem. Int. Ed. Engl. 60 (2021) 3299–3306, <https://doi.org/10.1002/anie.202012615>.
- [52] H. Yang, L. Gong, H. Wang, C. Dong, J. Wang, K. Qi, H. Liu, X. Guo, B.Y. Xia, Preparation of nickel-iron hydroxides by microorganism corrosion for efficient oxygen evolution, Nat. Commun. 11 (2020) 5075, <https://doi.org/10.1038/s41467-020-18891-x>.